Strain localization of rectangular clay specimen under undrained triaxial compression conditions

Localisation des déformations d'un spécimen parallélépipédique d'argile au cours d'essais de compressions triaxiales non-drainées

F. Oka, T. Kodaka, S. Kimoto & T. Ichinose
Department of Civil and Earth Resources Engineering, Kyoto University, Japan
Y. Higo
Geo-Research Institute, Osaka, Japan

ABSTRACT
In the present study, in order to grasp deformation and failure behaviors of clay under 3-D condition as well as large deformation and strain localization, a series of triaxial compression tests using rectangular clay specimens are performed. Various patterns of strain localization are successfully observed by an image analysis. 3-D bifurcation phenomena, e.g. formation and progress of various strain localization patterns, failure with buckling, unstable behavior in the stress-strain relations, can be also observed in the preset tests. Then, a 3-D finite element simulation using an elasto-viscoplastic model for a saturated clay is carried out. The simulated results can well explain the observed strain localization patterns of rectanguler clay sepcimens.

RÉSUMÉ
Dans la présente étude, afin de mieux comprendre tant le comportement en déformation et en rupture de l'argile en conditions tridimensionnelles que son comportement en grandes déformations et la localisation des déformations, une série de tests en compression uniaxiale sur des spécimens d'argile parallélépipédiques a été effectuée. Différentes formes de localisation des déformations ont été observées avec succès grâce à une analyse d'images. Le phénomène de bifurcation en 3D, telle que la formation et la propagation des différentes formes de localisation des déformations, la rupture par flambage, le comportement instable dans les relations contraintes-déformations ont également été observées au cours de ces essais. Enfin, une simulation 3D basée sur les éléments finis utilisant un modèle visco-plastique pour les argiles saturées a été mis en œuvre. On retrouve avec les résultats numériques les formes de localisation des déformations des spécimens parallélépipédiques d'argile.

1 INTRODUCTION

It is well-known that the strain localization of geomaterial is an important problem as an onsest of failure. The problem of strain localization in such geomaterials as soil and rock has been studied in the context of experimental, theoretical, and numerical approaches over the last three decades. However, it is mainly strain localization problems under plane strain conditions that have been discussed (e.g., Loret and Prévost 1991; Han and Vardoulakis 1991; Schrefler et al. 1996; Mokni and Desrues 1998; Oka et al. 2002; and Higo et al. 2004). In the natural ground, such strain localization phenomena as land slides involve three-dimensional shear bands. Thus, it is necessary to deal with strain localization phenomena under three-dimensional conditions. Kodaka et al. (2001) used rectangular clay specimens for the undrained triaxial compression tests, and studied three-dimensional strain localization with an image analysis of digital photographs taken during deformation. Using rectangular specimens, it is easy to set up the boundary conditions in a three-dimensional analysis. In addition, a quantitative comparison is possible through the distribution of shear strain obtained by the image analysis.

In the present study, undrained triaxial compression tests using rectangular specimens and their numerical simulation under three-dimensional conditions are conducted. In the experiments, both normally consolidated and overconsolidated clay samples are tested with different strain rates and different shapes and we carried out an image analysis in the same manner as that by Kodaka et al. (2001). The method of numerical simulation is a soil-water coupled three-dimensional finite element method with an elasto-viscoplastic model for water-saturated clay considering structural changes (Kimoto et al., 2004). Comparing the results of the experiment and the simulation, we have discussed the mechanism of three-dimensional strain localization.

2 TRIAXIAL COMPRESSION TEST FOR RECTANGULAR CLAY SPECIMENS

2.1 *Testing Program*

The clay used in the experiment is Fukakusa clay which is Pleistocene marine clay produced in the southeastern part of the Kyoto Basin. Liquid limit w_L =62%, plasticity index I_P =33, and the density of soil solid ρ_s =2.69g/cm^3. The specimens were consolidated one-dimensionally at a pre-consolidation pressure of 98 kPa. The clay specimens used in the triaxial tests were trimmed to rectangular shapes with different sizes (Fig.1). All specimens used in the present study were saturated by the double vacuum method and were acted upon by 200 kPa of back pressure. The normally consolidated clay specimens were isotropically consolidated to 200 kPa. The overconsolidated clay specimens were isotropically consolidated to 300 kPa, and then isotropically swelled to 50 kPa. After the consolidation or the swelling procedure, axial pressure was applied under undrained conditions by an axial loading device with an axial strain or displacement control system. We applied three axial strain rates monotonically in the tests. The test cases presented in this paper are listed in Table 1. Subscripts N and O indicate normally consolidated and overconsolidated clay respectively.

Table 1. Test cases

Case No.		strain rate (%/min)	size of specimen (cm)
A_O	1	1	4×4×12
	2	0.1	
	3	0.01	
B_N B_O	1	1	4×4×8
	2	0.1	
	3	0.01	

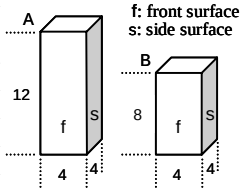

Figure 1. Shapes of the specimens (Unit: cm)

2.2 *Image Analysis*

We drew 2 mm square meshes on the rubber membranes covering the specimen (see Fig. 2). We took pictures from two sides of the specimens during the tests, then digitized the nodal coordinates of the meshes. Using the coordinates at the initial state and those of each axial strain level, the nodal displacements were calculated. Adopting the B matrix for the four-node isoparametric finite elements provides the strain of each element (see Higo, 2003 and Higo et al.). Finally we obtain distributions of the second invariant of deviatoric strain γ ($=\sqrt{e_{ij}e_{ij}}$, e_{ij} is the total deviatoric strain tensor). In the following, we call it 'shear strain γ', for simplicity.

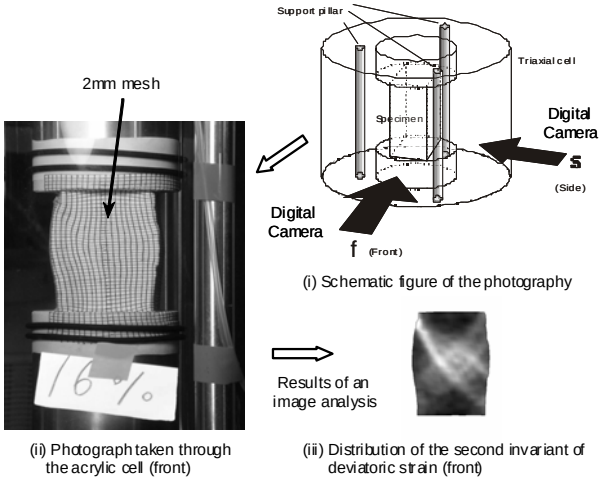

Figure 2. An example of the photographs taken through the acrylic cell and of results of an image analysis

2.3 *Experimetal results*

Distributions of shear strain γ for cases B_N-1 and B_O-1 are depicted in Fig. 3. The deformations are homogeneous until the axial strain reaches 4% of the axial strain, however, strain localization starts at 8% due to friction between the top and the bottom surfaces of the specimen and the test apparatus, and four shear bands are clearly seen at 12%. At an axial strain of 20%, two shear bands finally appear from the edge of the top and the bottom of the specimen, and shear bands are more clearly seen on one of the surfaces than the other.

Fig. 4 shows shows distributions of shear strain γ for specimen B with different strain rates at an axial strain of 20%. In the case of the fastest strain rate of 1%/min, shear bands develop from the top edge. On the other hand, in the case of the lowest strain rate of 0.01%/min, shear bands develop beneath the top edge. There are black areas, namely, areas where the shear strain is very small, near the top and the bottom ends. Shear band formation that is seen in the case of a middle strain rate of 0.1%/min starts from a relatively lower part than the top edge. Thickness of shear bands with lower strain rates is larger than that of bands with higher strain rates. In addition, we can observe larger numbers of shear bands in overconsolidated clay than those in normally consolidated clay.

The stress-strain relations for B_N cases are shown in Fig. 5. We can see the strain rate sensitivity with strain-hardening behavior until an axial strain of 12%, while those after 12% exhibit similar strain-softening behavior. This is probably because the deformation patterns with different strain rates are similar and the two clear shear bands from the top and the bottom edges clearly appear around an axial strain of 12%.

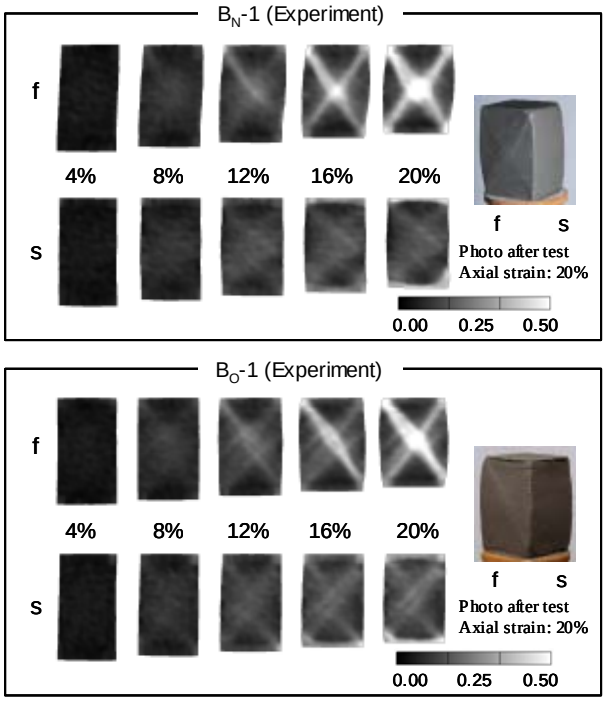

Figure. 3 Process of shear bands formation for B_N-1 and B_O-1 (Distributions of shear strain γ and photos after the tests)

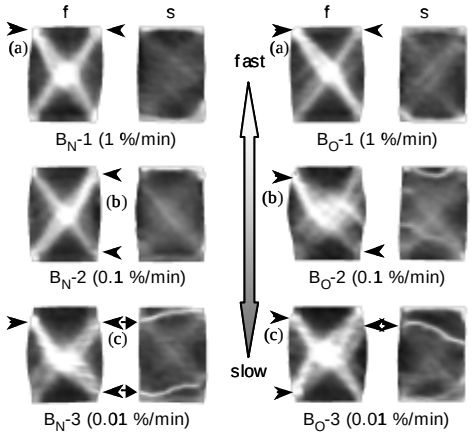

Figure 4. Distributions of shear strain γ for specimen B with different strain rates at an axial strain of 20%: (a) shear bands develop from the top edge, (b) shear bands develop just beneath the top edge, and (c) shear bands develop beneath the top edge.

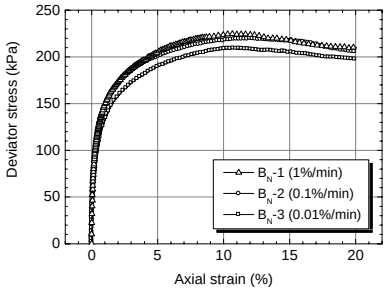

Figure 5. Stress-strain relations for B_N cases

Fig. 6 shows the results for A_O-1. Four shear bands from the top and the bottom edges of the specimen can be seen at an axial strain of 8% on both surfaces. However, only two shear

bands on the side surface grow and their thickness becomes large. We can see on the front surface that the intersection of the shear bands appears at an axial strain of 12%. This type of strain localization pattern just likes the buckling of a column as can be seen in the photographs.

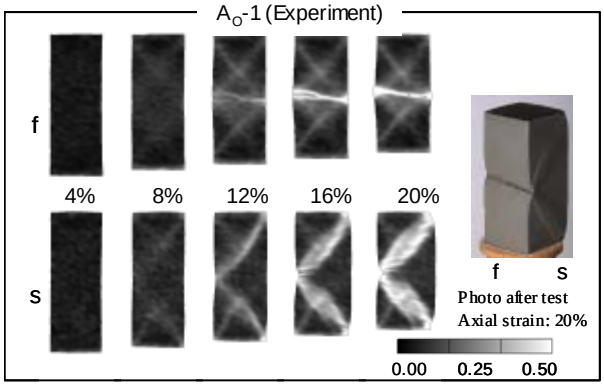

Figure 6. Process of shear bands formation for A_O-1 (Distributions of shear strain γ and photos after the tests)

Stress-strain relation and the process of shear bands formation for A_O-2 are demonstrated in Fig. 7. The deviator stress continues to increase until an axial strain of 9%, although strain localization is clearly seen at 8%. This is probably because the dilatancy of overconsolidated clay increases the deviator stress much more than the softening induced by development of the shear band on the side surface. When the strain softening behavior starts, the second shear band generates from 10% and intersects the first one. Finally, the second shear band becomes clearer than the other and the softening behavior continues up to 20%. In this way, the stress-strain relations of the cases of specimen A show strain softening corresponding the generation of shear bands.

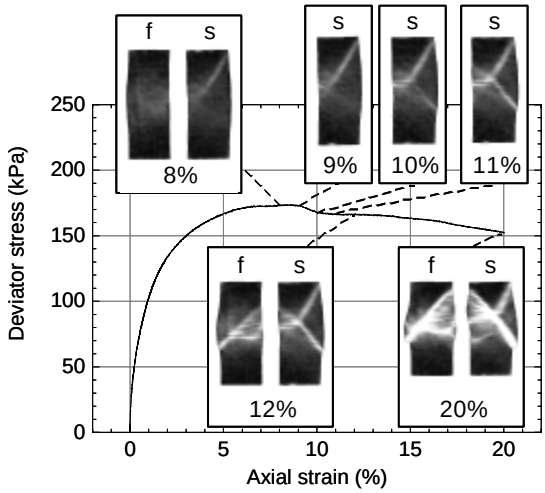

Figure 7. Stress-strain relation and the process of shear bands formation for A_O-2

3 NUMERICAL SIMULATION OF TRIAXIAL TESTS FOR RECTANGULAR CLAY SPECIMENS

For numerical simulation, we used a finite element method for two-phase mixtures based on the finite deformation theory. Biot's (1956) two-phase mixture theory is adopted to give the governing equations of the soil-water coupling problem. An updated Lagrangian method with the objective Jaumann rate of Cauchy stress is used for the weak form of the rate type of equilibrium equations for the soil-water whole mixture. For fluid phase, the weak form of continuity equation is employed. We adopted an elasto-viscoplastic constitutive model for water-saturated clay considering structural changes (Kimoto et al. 2004). The element types used in the three-dimensional analysis are a 20-node isoparametric element with a reduced Gaussian (2 × 2 × 2) integration for the soil skeleton and an 8-node isoparametric element with a full (2×2×2) integration for pore fluid are used. Detailed formulations for equilibrium equation and continuity equation are in the references, e.g., Oka et al. (1992), Higo (2003), and Higo et al. (2004).

Material parameters used in the analysis are listed in Table 1. They are determined by isotropic consolidation test, undrained triaxial compression tests with the different strain rates, and falling head permeability tests.

Table 1: Material parameters

Parameter		NC clay	OC clay
Compression index λ		0.191	0.191
Swelling index κ		0.043	0.043
Initial void ratio e_0		1.10	1.11
Compression yield stress σ'_{mbi}		200 (kPa)	300 (kPa)
Initial mean effective stress σ'_{m0}		200 (kPa)	50 (kPa)
Stress ratio at maximum compression M^*_m		1.14	1.14
Initial elastic shear modulus G_0	1 %/min	23400 (kPa)	13100 (kPa)
	0.1 %/min	17700 (kPa)	9920 (kPa)
	0.01 %/min	16300 (kPa)	9190 (kPa)
Coefficient of permeability k		1.63×10^{-9} (m/s)	2.86×10^{-9} (m/s)
Coefficient of earth pressure at rest K_0		1.0	1.0
Viscoplastic parameter C		5.8×10^{-10} (1/s)	2.7×10^{-9} (1/s)
Viscoplastic parameter m'		24.3	20.5
Structural parameter σ'_{maf}		170 (kPa)	270 (kPa)
Structural parameter β		10	5

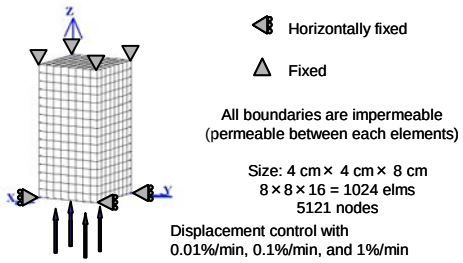

Figure 8. Boundary conditions

Boundary conditions used for the simulation are shown in Fig. 8. All the boundaries are assumed to be impermeable, however, the transport of pore water between each element is allowed. Constant displacements (z-direction) of 0.01%/min, 0.1%/min, and 1%/min are applied to the nodes on the bottom surface. As for the top and the bottom surfaces, frictional force occurs between the top and the bottom surfaces and the top cap and the pedestal. Consequently, we assumed that the horizontal (x-direction and y-direction) displacement of the nodes on both the top and the bottom surfaces is constrained.

Comparison between experimental results and simulation results for specimen B are demonstrated in Fig. 9. It can be seen that the localization modes and the effect of strain rate on the strain localization observed in the experiment are well reproduced by the simulation. We can see both in the experiment and in the simulation that the inclination angles of shear bands in the case with higher strain rate become larger than those with lower strain rate, and that the thickness of shear bands with lower strain rates is larger than that with higher strain rates

Distribution of pore water pressure for both normally consolidated clay and overconsolidated clay with different strain rate are depicted in Fig. 10. It can be seen that the distributions of pore water pressure with strain rate of 0.1%/min are rather homogeneous, since the difference between the maximum value and the minimum value is small. In the case with higher strain

rate of 1%/min, on the other hand, the difference is larger than that with lower strain rate of 0.1%/min, namely, pore water distributes heterogeneously in the specimen. We can say that migration of pore water can easily occur inside the specimen. It is worth noting that the distribution pattern of pore water pressure with higher strain rate of 1% and that of 0.1% are similar.

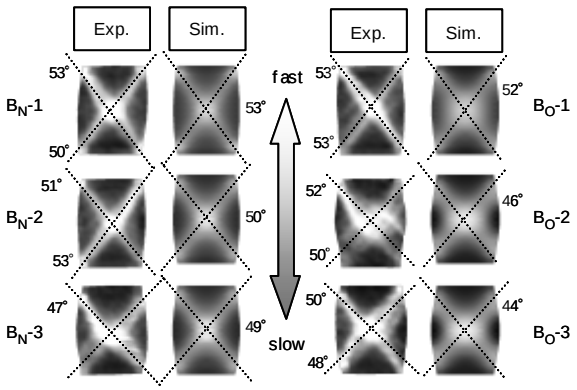

Figure 9. Comparison between experimental results and simulation results for specimen B (Distribution of shear strain γ, Axial strain: 20%)

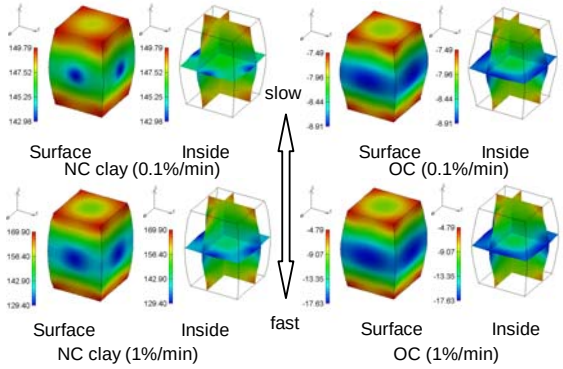

Figure 10. Distribution of pore water pressure (0.1%/min and 1%/min, Axial strain: 20%, Unit: kPa)

Figure 11 shows comparison between experimental results and simulation results for specimen A. In the case of A_O-1, the simulation well reproduce the development of four shear bands observed in the upper part and in the lower part of the specimen. The effect of the strain rates observed in the experiment, namely, the strains localize at the center part of the specimen in the case with lower strain rate, can be also seen in the simulation results.

In the experiment, we can see the asymmetric deformation modes. This is due to geometric imperfection and inherent material heterogeneity. Note that the simulation results are symmetric since we do not consider any geometric imperfection.

4 CONCLUSIONS

Three-dimensional strain localization of water-saturated clay has been investigated through the undrained triaxial compression tests for rectangular specimens. In addition, their numerical simulation by a soil-water coupled finite element analysis base on the large deformation theory with an elasto-viscoplastic constitutive model has been conducted. The strain localization behavior of both normally consolidated clay and overconsolidated clay has been carefully observed by an image analysis, and through the comparison between the experimental and the numerical simulation, it is found that the analysis method can well reproduce the not only three-dimensional strain localization of water-saturated clay but also the effect of the strain rates on the strain localization patterns.

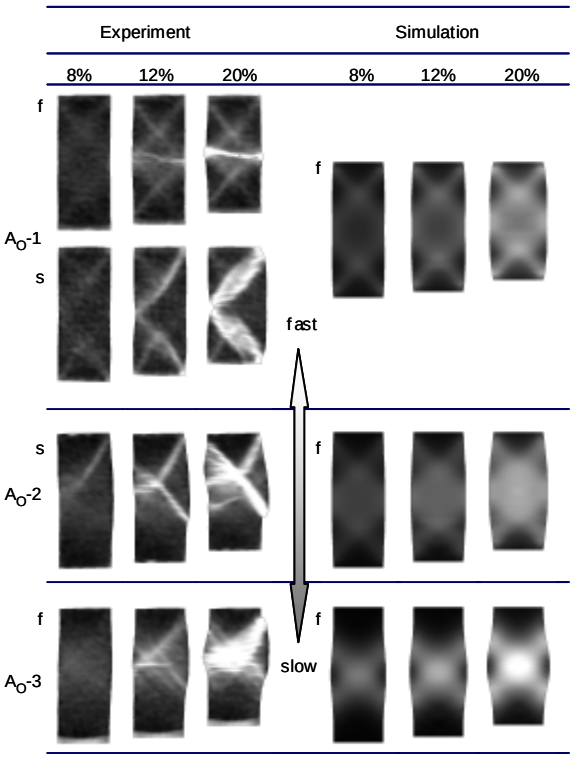

Figure 11 Comparison between experimental results and simulation results for specimen A (Distribution of shear strain γ, Axial strain: 20%)

REFERENCES

Adachi, T. and Oka F. 1982. Constitutive equations for normally consolidated clay based on elasto-viscoplasticity, *Soils and Foundations*, 22 (4), 55-70.

Han, C. and Vordoulakis, I. 1991. Plane-strain compression experiments on water saturated fine-grained sand, Géotechnique, 41 (1), 49-78.

Higo, Y. 2003. Instability and strain localization analysis of water-saturated clay by elasto-viscoplastic constitutive models. Doctoral thesis. Kyoto University, Japan.

Higo, Y., Oka, F., Jiang, M., and Fujita, Y. 2004. Effect of transport of water and material heterogeneity on strain localization analysis of fluid-saturated gradient-dependent viscoplastic geomaterial, *Int. J. Numerical and Analytical Methods in Geomechanics*, submitted.

Higo, Y., Oka, F., Kodaka, T., and Kimoto, S. 2004. Three-dimensional strain localization of water-saturated clay and numerical simulation using an elasto-viscoplastic model. *Philosophical Magazine*, submitted.

Kimoto, S., Oka, F., and Higo, Y. 2004. Strain localization analysis of elasto-viscoplastic soil considering structural degradation, *Comput. Methods Appl. Mech. Engrg.* 193, 2845-2866.

Kodaka, T., Higo, Y., and Takyu, T. 2001. Deformation and failure characteristics of rectangular specimens under three-dimensional condition, *Proc. 15th ICSMGE*, Istanbul, Balkema, 1, 167-170.

Loret, B. and Prévost, J.H. 1991. Dynamic strain localization in fluid-saturated porous media. *J. Eng. Mech.*, ASCE, 11, 177-190.

Mokni, M. and Desrues, J. 1998. Strain localization measurements in undrained plane strain biaxial tests on Hostun RF sand, *Mech. of Cohesive-Frictional Materials*, 4, 419-441.

Oka, F., Yashima, A., and Kohara, I. 1992. A finite element analysis of clay foundation based on finite elasto-viscoplasticity, Proc. 4th Int. Symposium on Numerical Models in Geomechanics, Swansea, Pande, G.N. and Pietruszczak, S. eds., 2, Balkema, 915-922.

Oka, F., Higo, Y., and Kimoto, S. 2002. Effects of dilatancy on the strain localization of water-saturated elasto-viscoplastic soil. *Int. J. Soilds and Structures*, 39, 3625-3647.

Schrefler, B.A., Sanavia, L., and Majorana, C.E. 1996. A multiphase medium model for localization and postlocalization simulation in geomaterials, *Mech. of Cohesive-Frictional Materials*, 1, 95-114.